Spoof-Surface-Plasmon-Polariton Metawaveguide and its Application in Frequency-Shift Keying

Yi Fan[1,2,*,§] Pei Hang He,[1,2,§] Ling Yun Niu,[1,2] Yang Zhao,[1] Hao Chi Zhang,[1,2,†] and Tie Jun Cui[1,2,‡]

[1]*The State Key Laboratory of Millimeter Waves, Southeast University, Nanjing 210096, China*

[2]*Institute of Electromagnetic Space, Southeast University, Nanjing 210096, China*

Spoof-surface-plasmon polaritons (SSPPs) supported by artificial microwave metawaveguides can mimic other properties of optical-surface-plasmon polaritons (SPPs) and have the potential to build the next generation of circuits and systems. However, the traditional model of SSPP metawaveguides take only physical characters of electrical length and characteristic impedance into consideration and thus can hardly guide the design of integrated SSPP systems efficiently. In this work, a modified model of SSPP metawaveguide is proposed to realize multicharacteristic optimization design of integrated SSPP systems. To validate the modified model, a SSPP-based frequency-shifting keying (FSK) modulation and demodulation system is realized. In comparison to microstrips and SSPP metawaveguides based on the traditional model, the SSPP metawaveguides based on the modified model bring lower discontinuity, lower coupling, and lower system complexity to the FSK modulation and demodulation system, which improves the quality of demodulated signals significantly. Hence, exploring physical characteristics of SSPP metawaveguides by introducing modified models is an effective route to realize outstanding integrated SSPP systems.

I. INTRODUCTION

Surface-plasmon polaritons (SPPs) [1] are kinds of surface waves confined on the metal-dielectric interface at subwavelength scale and decay exponentially in the direction perpendicular to the interface and can be widely applied in optoelectronics [2], the Janus emitter [3], and biosensors [4,5]. However, SPPs cannot naturally be supported at lower frequencies because the metal behaves like a perfect electric conductor instead of plasma with negative permittivity in the microwave band. Hence, metamaterials [6–11] are used to support the spoof-surface-plasmon polaritons (SSPPs) [12], which can mimic the property of SPPs. SSPPs can be supported by metamaterials with periodically decorated metallic structures, also called the SSPP metawaveguide [13–17]. Due to the outstanding merits of field confinement [18,19] and slow-wave property [15], SSPP metawaveguides have been demonstrated to realize many single devices, including amplifiers [20,21], harmonic generators [22,23], filters [24–27], antennas [28–35], and modulators [36–38]. Recently, a SSPP-based sensor network [39] and wireless communication systems [40]

have been reported, which imply the potential of SSPPs in building the next-generation systems.

To guide the design of high-performance integrated SSPP systems, a powerful model of SSPP metawaveguides is necessary to guarantee satisfying circuit-matching and field-confinement performances. However, the traditional model [13–15] of SSPP metawaveguides describes the circuit-matching performance by only characteristic impedance [41] and field-confinement performance by only electrical length. On one hand, not only the characteristic impedance but also the geometrical discontinuity should be considered for circuit matching. On the other hand, field confinement depends on the wave number rather than the electrical length. The achievements of SSPPs mentioned above are mainly based on the traditional model and are still far away from reaching the upper limit of the potential of SSPP metawaveguides. Therefore, a model with more dimensions is still needed to explore the potential of SSPP metawaveguides.

In this paper, we propose a modified model of SSPP metawaveguides to describe the circuit-matching performance and field-confinement performance completely. Both characteristic impedance and geometrical discontinuity are considered in the modified model so that satisfying circuit matching can be realized. A more appropriate method to describe field-confinement performances is also presented in this model. Based on the modified model of a

* 547173457@qq.com

† hczhang0118@seu.edu.cn

‡ tjcui@seu.edu.cn

§ Yi Fan and Pei Hang He contributed equally to this work.

SSPP metawaveguide, a frequency-shifting keying (FSK) modulation and demodulation system with the advantages of low discontinuity, low coupling, and low system complexity is realized, which demonstrated the value of this modified model.

A brief overview of this paper is now described. Firstly, a modified model of SSPP metawaveguides, which can realize satisfying circuit-matching and field-confinement performances is proposed. Then, a SSPP-based FSK modulation and demodulation system is implemented under the guidance of the modified model. At last, samples of SSPP-based systems and microstrip-based systems are fabricated and compared to demonstrate the advantages of the modified model of SSPP metawaveguides.

II. MODELS OF SSPP METAWAVEGUIDES WITH SRRS

An adequate model of SSPP waveguides is the key to design high-performance integrated SSPP systems. The traditional model of SSPP metawaveguides is composed of a microstrip and a shunt open stub [32], as shown in Fig. 1(a). In the traditional model, only the characteristic impedance Z_e is used to guide the design of circuit matching, which ignores the geometrical discontinuity in cascaded networks. Meanwhile, only the equivalent electrical length θ_e of the SSPP metawaveguide is used to describe the field-confinement performances, which is inaccurate because enough electrical length can also be achieved by a longer waveguide with weaker field confinement.

To guide the design of integrated multifunctional SSPP systems, we propose a modified model as shown in Fig. 1(b), where a *LC* resonator is used to provide more freedom degrees of the passband. The *ABCD* matrix of the modified model SSPP metawaveguide unit can be expressed by

$$
\begin{bmatrix} A & B \\ C & D \end{bmatrix} = \begin{bmatrix} \cos\theta_e & jZ_e\sin\theta_e \\ jY_e\sin\theta_e & \cos\theta_e \end{bmatrix}
$$

$$
= \begin{bmatrix} \cos\theta_s(l_s) & jZ_s(w_s)\sin\theta_s(l_s) \\ jY_s(w_s)\sin\theta_s(l_s) & \cos\theta_s(l_s) \end{bmatrix} \begin{bmatrix} 1 & 0 \\ jb & 1 \end{bmatrix} \times \begin{bmatrix} \cos\theta_s(l_s) & jZ_s(w_s)\sin\theta_s(l_s) \\ jY_s(w_s)\sin\theta_s(l_s) & \cos\theta_s(l_s) \end{bmatrix}, \quad (1)
$$

where the b is the reactance of the shunt open stubs and *LC* resonator, the θ_s and Z_s are the phase shift and characteristic impedance of the microstrip, the θ_e and Z_e are the equivalent electrical length and characteristic impedance of the SSPP metawaveguide, the l_s is the length of the SSPP waveguide unit and w_s is the port width of the SSPP metawaveguide, respectively. b can be further calculated by

$$
b = \frac{1/(Z_b\cot\theta_b)\times(j\omega C+1/j\omega L)}{1/(Z_b\cot\theta_b)+(j\omega C+1/j\omega L)}, \quad (2)
$$

where θ_b and Z_b are the electrical length and characteristic impedance of the microstrip, respectively. It should be noted that if a simply SSPP waveguide without the *LC* resonator structure is analyzed, the modified model is still valid as long as values of L and the C are set as 0.

And the dispersion relation of the SSPP metawaveguide can be calculated by

$$
\cos\theta_e = \cos 2\theta_s(l_s) - \frac{bZ_s(w_s)\sin 2\theta_s(l_s)}{2}. \quad (3)
$$

Then, to describe the field confinement of SSPP waveguides, a variable D named confinement factor is proposed

and can be calculated by

$$
D = \frac{\theta_e}{2\theta_s(l_s)} = \frac{\cos^{-1}[\cos 2\theta_s(l_s) - bZ_s(w_s)\sin 2\theta_s(l_s)/2]}{2\theta_s(l_s)}, \quad (4)
$$

which indicate that the field confinement of SSPP waveguides mainly depends on the ratio of the equivalent electrical length to the electrical length of the fundamental transmission medium. Then, the equivalent characteristic impedance Z_e of the SSPP metawaveguide can be calculated by

$$
Z_e = \frac{Z_s(w_s)[\sin 2\theta_s(l_s) - bZ_s(w_s)\sin^2\theta_s(l_s)]}{\sin\theta_e}. \quad (5)
$$

Based on Eq. (5), the SSPP metawaveguides cannot transmit electromagnetic waves when

$$
\frac{Z_s(w_s)[\sin 2\theta_s(l_s) - bZ_s(w_s)\sin^2\theta_s(l_s)]}{\sin\theta_e} = 0, \quad (6)
$$

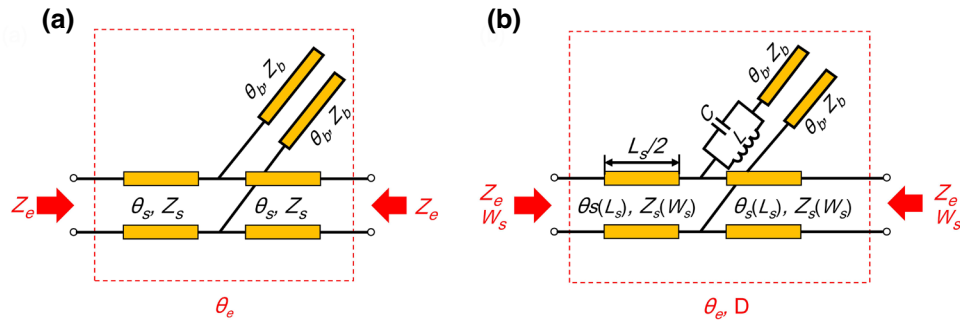which can be realized at the resonant frequency and cutoff frequency of the SSPP waveguide.

FIG. 1.   (a) The circuit model of the typical SSPP metawaveguides. (b) The new circuit model of SSPP metawaveguide.

III. THE SYSTEM OF MODULATION AND DEMODULATION

A typical modulation and demodulation system based on the microstrip is shown in Fig. 2(a). A voltage-control oscillator (VCO) is used to generate binary FSK signals through the "0" and "1" signal in the modulator. To transmit the generated binary FSK signals, a 50-Ω microstrip with fixed line width is connected to the pin of the VCO chip and a filter is needed to eliminate harmonics, where the geometrical mismatch will lead to discontinuity.

The commonly used demodulation methods for binary FSK modulation include coherent demodulation and noncoherent demodulation [42]. Since the coherent demodulation needs to add additional circuits to recover the carrier, the complexity of the system will be increased. Therefore, we focus our study on noncoherent demodulation to restore the signal in this work. In fact, most of the conclusions in the following designs can also be applied to coherent demodulation. In the demodulator, binary FSK signals are divided into two channels by a frequency divider realized by two band-pass filters with different working frequencies. Then the two different carrier signals can be sent to two envelope detectors separately for final information reading.

In comparison to the microstrip-based system, the system based on the modified model of SSPPs has outstanding advantages shown in Fig. 2(b). In the design of SSPP-based FSK modulator, the characteristic impedance of the SSPP metawaveguide is decided by the characteristic impedance of VCO. In addition, the port width of the SSPP metawaveguide should be matched with the small pin of the VCO to eliminate geometric discontinuity.
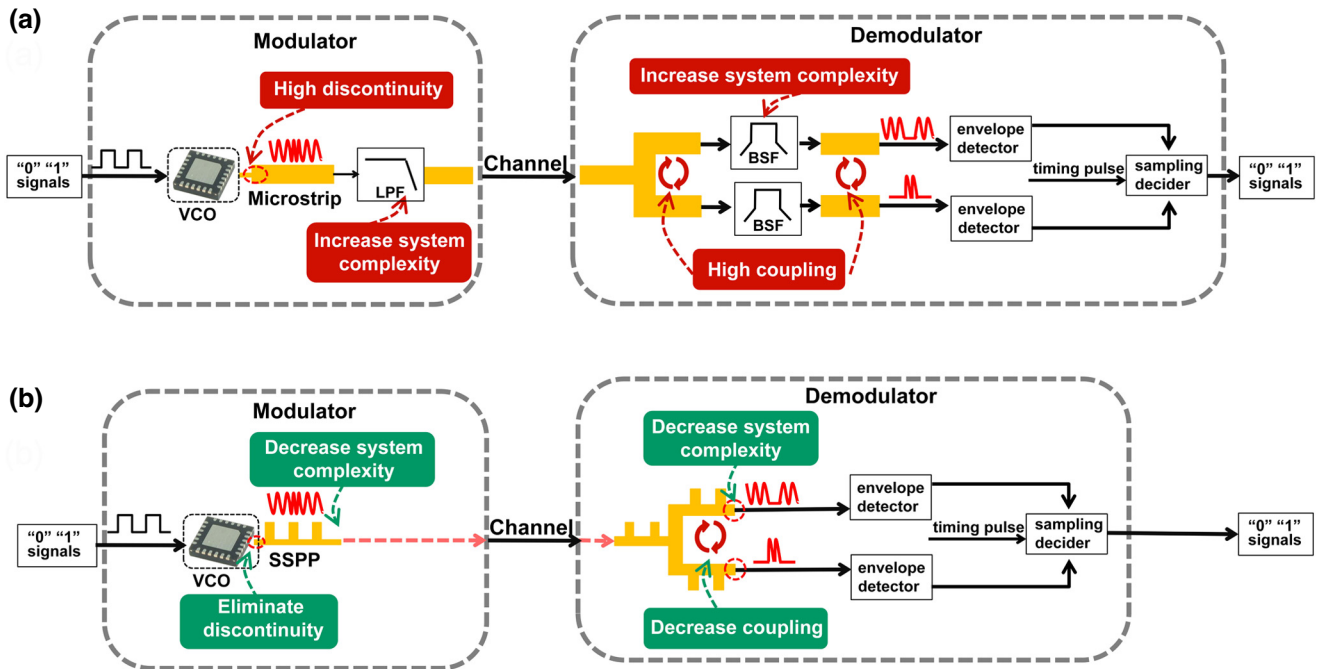

FIG. 2.   (a) Modulation and demodulation architecture based on microstrip. (b) Modulation and demodulation architecture based on SSPP.
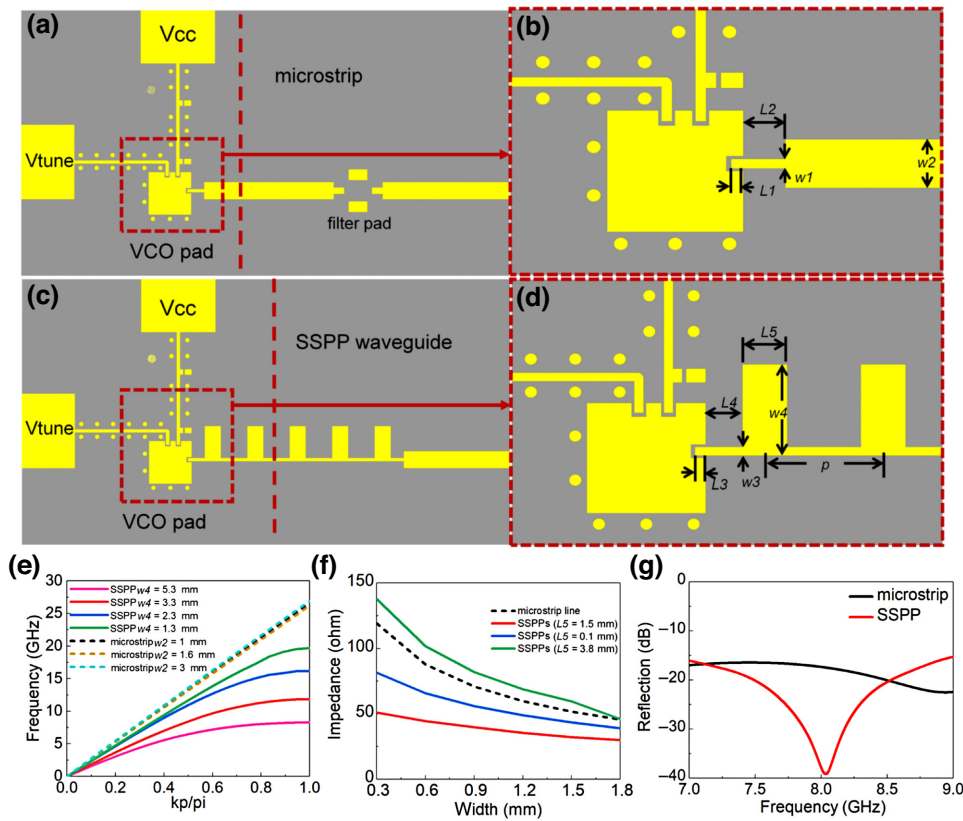
FIG. 3. Modulator structures. (a) Modulator based on microstrip. (b) The VCO pad connected to microstrip. (c) Modulator based on SSPP waveguide, (d) the VCO pad connected to SSPP waveguide. (e) The dispersion freedom of SSPP waveguide compared to the microstrip line. (f) The impedance freedom of the SSPP waveguide compared to the microstrip line. (g) Reflection between the pin of VCO and 50-Ω microstrip and SSPP waveguide.

In the modulator, the port of 50-Ω SSPP waveguide can be modified into an identical size to the pins by the modified model of SSPPs so that they can be connected without discontinuity loss. Due to the dispersion freedom of SSPPs, the harmonic filter is not needed in the SSPP-based system. In the demodulator, the SSPP frequency divider has lower coupling due to the field distribution freedom of SSPPs. Hence, using the extensive freedom of SSPPs to design the FSK modulation and demodulation system can significantly improve system performance and realize more compact size simultaneously.

A. Design of modulator

A VCO chip on the SSPP waveguide is used to generate the controlled binary FSK signals. Compared to FSK modulators based on diodes [38,39], the VCO option provides higher power efficiency and frequency continuous tunability, which can result in better performance in terms of power and flexibility. There is a corresponding relationship between the output frequency and the input control voltage for VCO. Thus, the binary FSK signals can be generated by inputting digital control voltages. Meanwhile, to solve the problem of geometrical discontinuity between the waveguide and VCO chip, the equivalent characteristic impedance and port width in the modified model of the

SSPP metawaveguide should meet

$$Z_e = Z_{\text{VCO}} \tag{7}$$

and

$$w_s = w_{\text{VCO}}, \tag{8}$$

where Z_{VCO} and w_{VCO} are port impedance and pin width of the VCO chip.

To realize modulation and demodulation at microwave frequencies, HMC506LP4 is selected as the VCO and the frequency range is 7.2–8.7 GHz. The modulator based on the microstrip and SSPP waveguide are shown in Figs. 3(a) and 3(c), respectively. The VCO pads to connect the SSPP
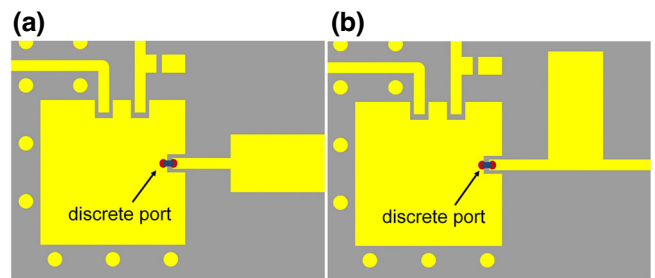

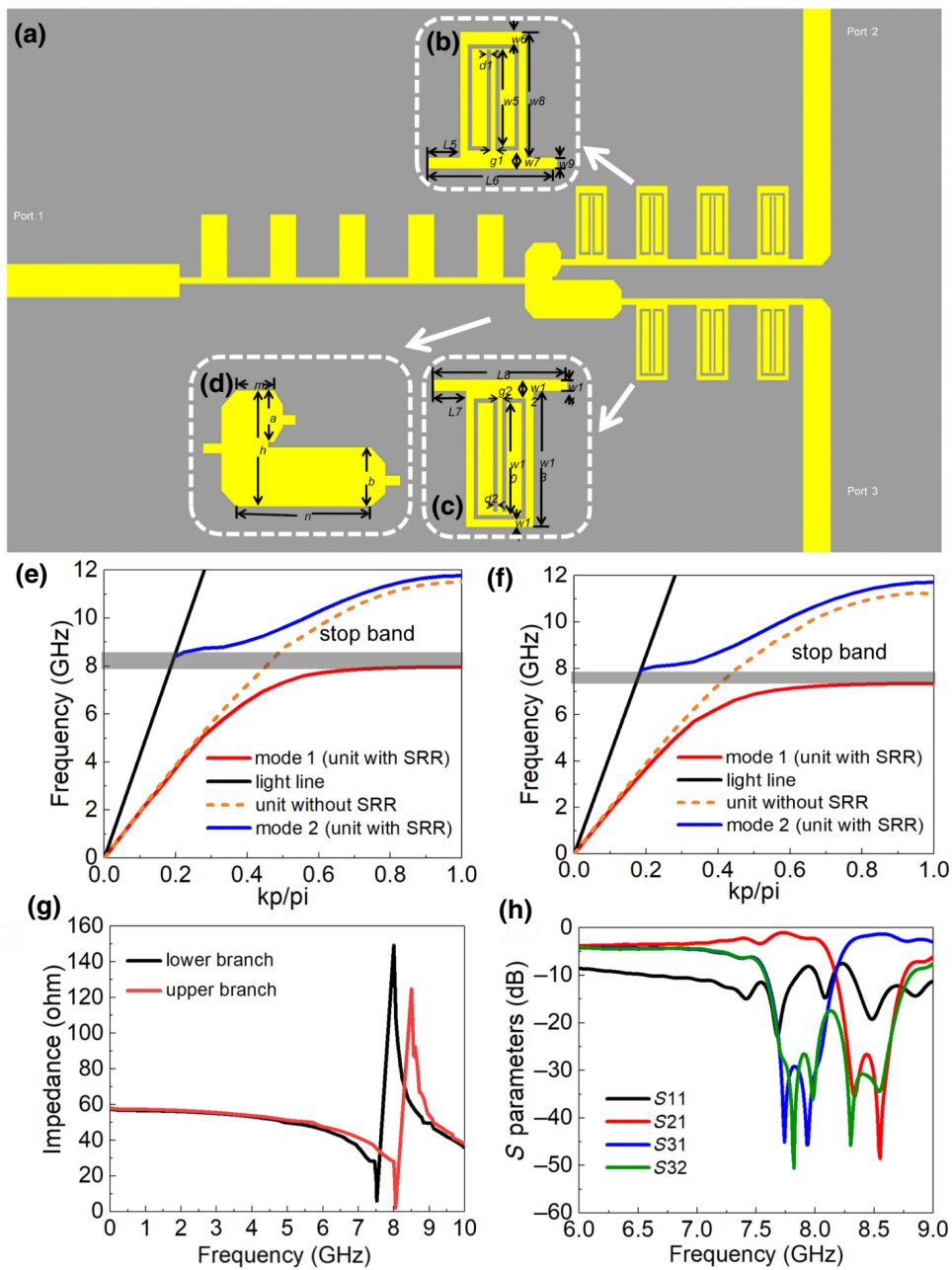FIG. 4. The discrete ports of (a) microstrip and (b) SSPP waveguide.

FIG. 5. Demodulator structure based on SSPP waveguide. (a) The demodulator based on SSPPs. (b) Unit of the upper branch. (c) Unit of the lower branch. (d) T-shaped structure of the frequency divider. The dispersion curves of (e) the upper branch and (f) the lower branch. (g) The relationship curves between the impedance and frequency of the two branches. (h) Simulated S parameters of the frequency divider based on the SSPP waveguide.

waveguide and the microstrip line can be observed in Figs. 3(b) and 3(d). The dimensions shown in Figs. 3(b) and 3(d) are $L_1 = 0.35$ mm, $L_2 = 1.25$ mm, $w_1 = 0.3$ mm, $w_2 = 1.59$ mm, $L_3 = 0.35$ mm, $L_4 = 1.25$ mm, $L_5 = 1.5$ mm, $p = 4$ mm, $w_3 = 0.3$ mm, and $w_4 = 3.3$ mm.

It can be obviously found that there is a geometrical mismatch between a small pin and the 50-Ω microstrip with fixed line width in Fig. 3(b). To demonstrate the difference of impedance freedom between the microstrip and SSPP

waveguide, the relationship curves between the impedance and total line width of the microstrip line and SSPP waveguide with different parameters are shown in Fig. 3(f). It can be observed that the impedance of the microstrip is determined by the width of the microstrip when the substrate is decided. And the impedance of SSPPs can be controlled freely by multiple parameters. Figure 3(f) demonstrates the manipulation ability of impedance of SSPPs by adjusting $L5$ as an instance with the guidance of the modified model.

In addition, dispersion curves of the SSPP waveguide and microstrip line with different parameters are shown in Fig. 3(e). It shows that the dispersion curve of the microstrip is hard to control by line width but easy to control by the SSPP metawaveguide. And this large geometric discontinuity increases the reflection loss, as shown in Fig. 3(g). The simulation ports' setting is shown in Fig. 4. Different from the microstrip-based system, utilizing the modified model of SSPPs, port width of the 50-Ω SSPP waveguide can be adjusted with the same substrate, so that the impedance and geometric size can be matched at the same time, as shown in Fig. 3(g). Meanwhile, the dispersion freedom of the SSPP waveguide can be utilized to suppress harmonics effectively. The SSPP waveguide can be equivalent to a low-pass filter with 12-GHz cutoff frequency. The inherent filtering property reduces the system complexity and reduces structure discontinuity.

B. Design of demodulator

The main structure of demodulator is the SSPP-based frequency divider, which is traditionally realized by the dispersion freedom of SSPPs. Since a split-ring-resonator (SRR) structure was proposed [43], it has been verified that SRR can produce negative equivalent permeability in a specific frequency band, thereby inhibiting

FIG. 7. Photographs of the fabricated (a) modulator and (b) demodulator based on SSPP waveguide. Photographs of the fabricated (c) modulator and (d) demodulator based on microstrip. (e) The spectrum test system and (f) the oscilloscope test system.

the propagation of electromagnetic waves [44]. It can not only be used as a unit of metamaterials but also be applied to realize filtering function. Filters based on SRR have the advantages of miniaturization, high integration, and easy processing. So, loading SRRs on the SSPP waveguide is considered to design the frequency divider, as shown in Fig. 5(a). The dimensions of the SSPP units with SRRs shown in Figs. 4(b) and 4(c) are
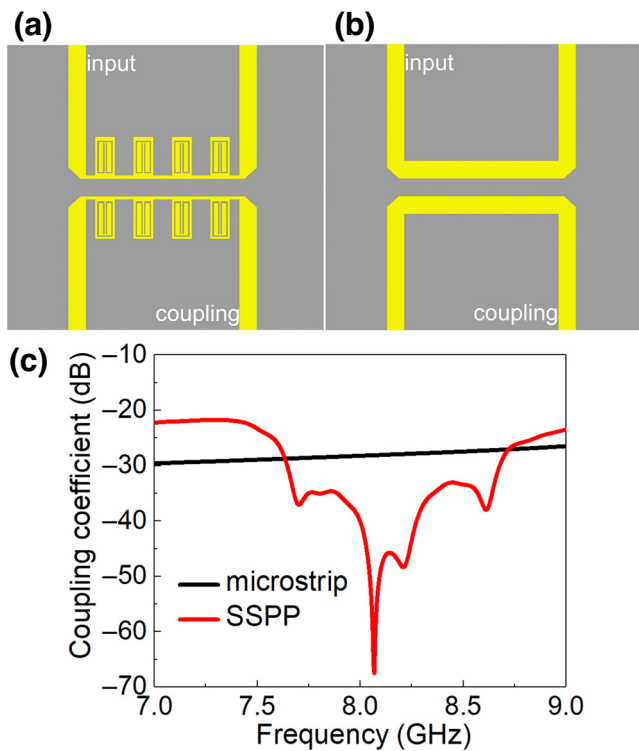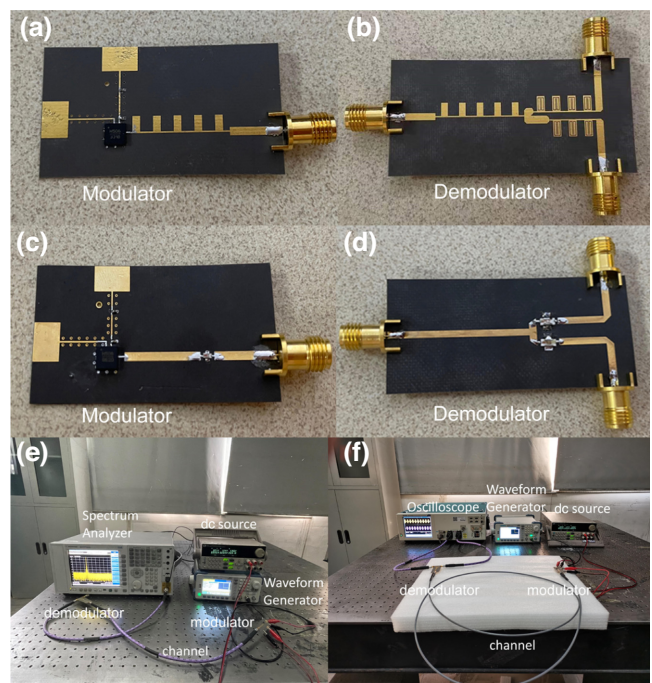

FIG. 6. The couplers based on the upper and lower branches of the (a) SSPP waveguide and (b) microstrip frequency dividers. (c) The simulated coupling of the frequency dividers based on the microstrip and SSPP.
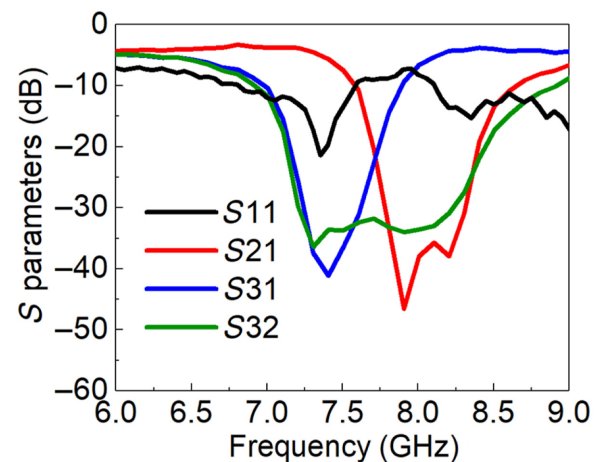

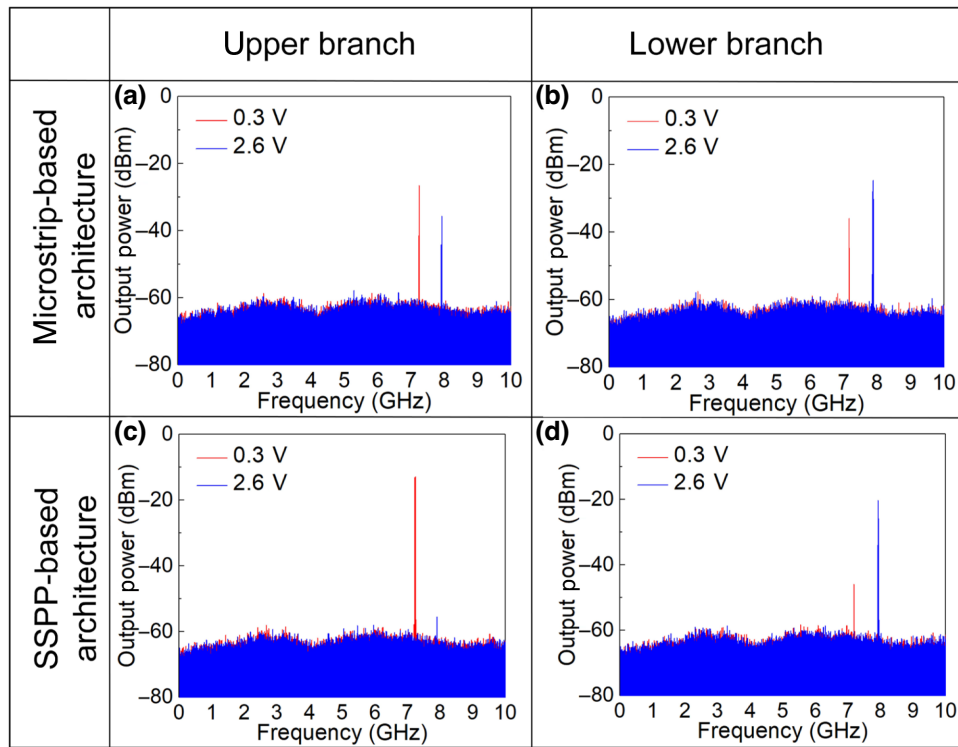FIG. 8. Measured *S* parameters of the frequency divider based on SSPPs.

FIG. 9. Measured spectra of (a) upper branch and (b) lower branch of the microstrip with voltage 0.3 and 2.6 V. Measured spectra of the (c) upper branch and (d) lower branch of the SSPP with voltage 0.3 and 2.6 V.

$g_1 = 0.12$ mm, $d_1 = 0.12$ mm, $L_5 = 0.85$ mm, $L_6 = 3.5$ mm, $w_5 = 2.71$ mm, $w_6 = 0.35$ mm, $w_7 = 0.5$ mm, $w_8 = 3.5$ mm, $w_9 = 0.3$ mm, $g_2 = 0.12$ mm, $d_2 = 0.12$ mm, $L_7 = 0.85$ mm, $L_8 = 3.5$ mm, $w_{10} = 2.96$ mm, $w_{11} = 0.2$ mm, $w_{12} = 0.5$ mm, $w_{13} = 3.6$ mm, and $w_{14} = 0.3$ mm. The dispersion curves of the SSPP units with SRRs are shown in Figs. 5(e) and 5(f). It can be obviously observed that there would be a stop band between the dispersion curves of the two modes of SSPPs caused by the loading SRRs, and the stopbands can be adjusted by the dimension of the SRRs.

The difficulty in designing the frequency divider is the impedance matching of the T-shaped structure. And utilizing the modified model can perfectly overcome this problem. The relationship curve between impedance and frequency of the SSPP units with SRRs is shown in Fig. 5(g). It can be observed that there is a maximum point and a minimum point of impedance in the impedance and frequency relationship curves of the upper and lower branches. And the frequency band between the minimum point and the maximum point of impedance is exactly the stopband of the upper and lower branches. It can be inferred that there is a short-circuit point in the first half of the equivalent circuit of the stopband and an open-circuit point in the second half based on the dispersion curves of both the upper and lower branches. As shown in Fig. 5(f), for the lower branch, the stopband lower than 7.7 GHz is generated by the short-circuit point, and the stopband higher than 7.7 GHz is generated by the open-circuit point. The same is true for the upper branch in Fig. 5(e). The modified model guides the impedance matching of

the T-shaped structure. The upper branch's open-circuit point (around 7.7 GHz) and the lower branch's short-circuit point (around 8.4 GHz) are selected for impedance matching. In order to realize the function of frequency division, it is necessary to ensure that the impedance of one branch is matched and the other branch is equivalent to an open circuit, respectively. Thus, the upper branch is matched with 50 Ω when the short-circuit lower branch is equivalent to an open circuit through a quarter-wavelength impedance converter at about 7.7 GHz. Similarly, when the lower branch is matched with 50 Ω at about 8.4 GHz, the upper branch is equivalent to an open circuit. The final design of the T-shaped structure is shown in Fig. 5(d). The dimensions are $h = 3.605$ mm, $a = 1.6$ mm, $b = 1.834$ mm, $m = 1.29$ mm, and $n = 4.6$ mm. Moreover, coupling of frequency divider branches can be significantly reduced utilizing the field distribution freedom of SSPPs. As shown in Fig. 5(d), the distance between the upper and lower branches of the frequency divider is too small, and there may be serious coupling. The coupling of the two branches decreases the isolation, thereby increasing the bit-error rate. Because SSPPs has the characteristic of strong field confinement, the coupling degree of SSPPs is lower than that of the microstrip when they are connected to the same T-shaped structure. We simulate the couplers based on the upper and lower branches of the microstrip and SSPP frequency divider to verify this assumption.

In order to be closer to the coupling degree of the working state of the frequency divider, the distance of the coupler's branches is consistent with the T-shaped structure.
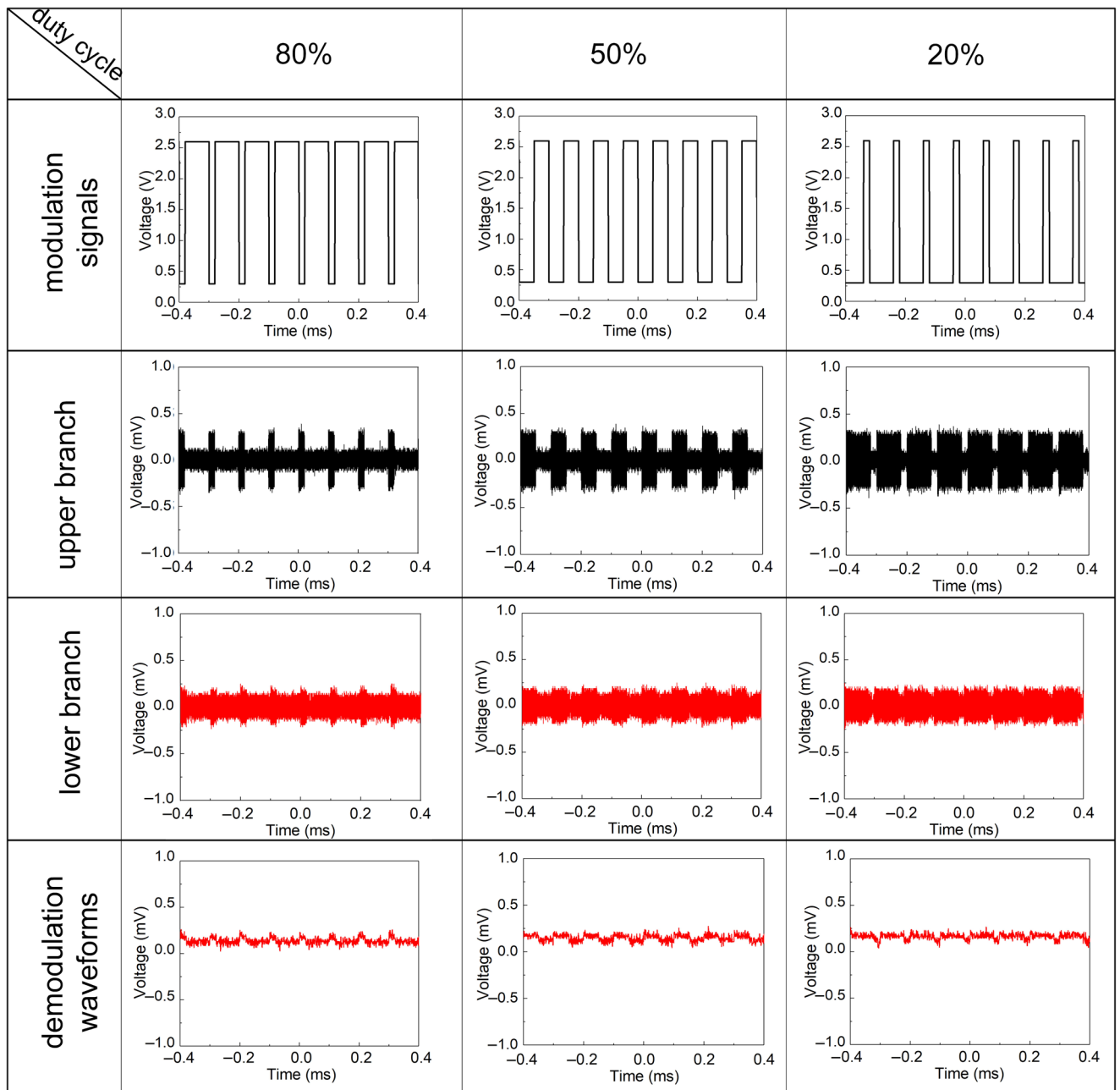
FIG. 10.   Modulation signals and measured demodulation waveforms of the microstrip-based system with different duty cycle.

The models of the microstrip coupler and SSPP coupler are shown in Figs. 6(a) and 6(b), respectively. It is easy to see that the branches based on SSPPs have much smaller coupling in Fig. 6(c). The simulated result of the frequency divider is shown in Fig. 5(h). This equivalent short- and open-circuit point design makes the SSPP frequency divider achieve high isolation ($S32$) and low reflection ($S11$). It can be observed that the reflection is significantly reduced at 7.7 and 8.4 GHz, which demonstrates that the branches have achieved very good matching with the SSPP waveguide at 7.7 and 8.4 GHz. It means that the

best matching points are 7.7 and 8.4 GHz. Thus, Fig. 5(h) shows that the frequency divider has an excellent performance when separating two signals with different frequencies with the design guidance of the modified model of SSPPs.

IV. EXPERIMENTS

To demonstrate the superior performance of the SSPP-based binary FSK modulation and demodulation system by the guidance of modified model experimentally, two
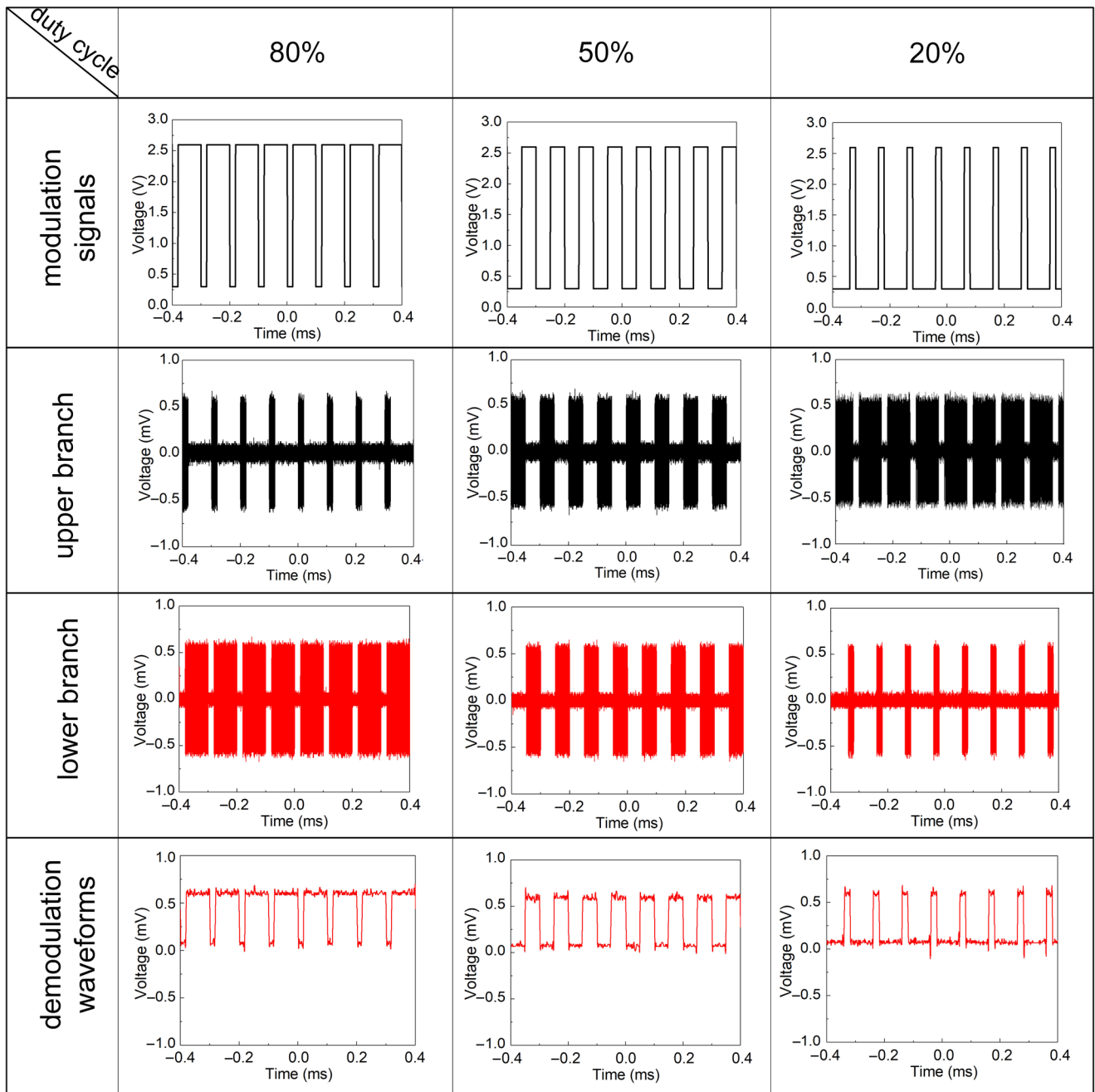
FIG. 11.   Modulation signals and measured demodulation waveforms of the SSPP-based system with different duty cycle.

samples of all SSPP-based systems and microstrip-based systems, as shown in Figs. 7(a)–7(d), are tested in the same environment. Measured S parameters of the frequency divider based on SSPPs is shown in Fig. 8. This figure shows that the two frequency points with the best matching of the upper and lower branches are about 7.3 and 8.2 GHz. Compared with the simulated results, the best matching point of the test has a slight frequency deviation, which is possibly caused by fabrication errors or simulation accuracy issues. The overall good performance,

including high transmission efficiency, low reflection, and high isolation of the SSPP-based frequency divider can be easily observed. The whole modulation and demodulation process is tested as well. The VCO in the modulator can produce waves at 7.3 and 8.2 GHz by offering amplitude of 0.3- and 2.6-V square waves with different duty cycle. The modulator output signals are sent to the frequency dividers whose upper and lower branches are connected to the spectrum analyzer, respectively. The photo of the measurement environment is shown in Fig. 7(e). It should be noted that

TABLE I.   The performance comparison of FSK modulation based on SSPPs.

	This work	[37] SCIS′20	[38] Nanophotonics′21
Frequency source	VCO	Diodes	Diodes
Efficiency	Highest	Low	Higher
Freq. continuous tunability	Yes	No	No
Geometric discontinuities	No	Yes	Yes
FSK demodulation	Yes	No	No

when testing with a spectrum analyzer, we connect a 20-dB attenuator to protect the instrument. The output spectrum of the demodulators are shown in Fig. 9. The output power difference of the same branch of the microstrip demodulator for the two signals is less than 10 dB. But the output power difference between the upper and lower branches of the SSPP demodulator for the two signals is about 43 and 25 dB, respectively. In order to visually display the demodulated waveform, we use the oscilloscope (DPO75902SX) to connect the upper and lower branches of the frequency divider, as shown in Fig. 7(f). The final output waveforms with different duty cycles from the microstrip-based and SSPP-based demodulator are shown in Figs. 10 and 11, respectively. It can be observed easily that the microstrip-based system cannot completely demodulate the waveform in Fig. 10 due to the strong coupling and high discontinuity. But the waveform amplitude of all SSPP-based system is almost 3 times that of microstrip-based, which indicates a lower bit-error rate in wireless communication. These results demonstrate that the FSK modulation and demodulation system can effectively break the limitations of the traditional systems with the guidance of the modified model, significantly improve the performance and realize compact architecture.

In addition, the table of performance comparison of the FSK modulator based on SSPPs are given in Table I. It can be observed in Table I, which compared with the existing FSK modulators. Diode-based FSK modulator can cause sudden phase changes of the generated FSK signals and inevitably wastes energy of the spare frequency source. However, this work can realize continuously tunable frequency by using a high-efficiency VCO-based FSK modulator. Additionally, with the method of eliminating geometric discontinuity, the VCO-based FSK modulator has the lowest reflection. This work proposed a complete SSPP FSK modulation and demodulation system with the best overall performance.

V. CONCLUSIONS

We propose a modified model to design integrated SSPP-based systems. The SSPP-based system and a microstrip-based one are compared to exhibit the superior performance of the SSPP-based system, including lower discontinuity, lower coupling, and lower system complexity, which breaks the limitations caused by traditional

system effectively. Hence, the SSPP-based system demonstrated that the modified model of SSPP metawaveguide can realize multicharacteristic optimization design of integrated SSPP systems.

[1] W. L. Barnes, A. Dereuxand, and T. W. Ebbesen, Surface plasmon subwavelength optics, Nature **424**, 824 (2003).

[2] H. Q. Zhang, B. Abhiraman, Q. Zhang, J. S. Miao, J. Kiyoung, S. Roccasecca, M. W. Knight, A. R. Davoyan, and D. Jariwala, Hybrid exciton-plasmon-polaritons in van der Waals semiconductor gratings, Nat. Commun. **11**, 1 (2020).

[3] S. Y. Heo, G. J. Lee, H. Kim, Y. J. Kim, S. Ishii, M. S. Kim, T. J. Seok, B. J. Lee, H. Lee, and Y. M. Song, A Janus emitter for passive heat release from enclosures, Sci. Adv. **6**, 36 (2020).

[4] V. S. Chaudhary, D. Kumar, and S. Kumar, Gold-immobilized photonic crystal fiber-based SPR biosensor for detection of malaria disease in human body, IEEE Sens. J. **21**, 16 (2021).

[5] V. S. Chaudhary, D. Kumar, G. P. Mishra, S. Sharma, and S. Kumar, Plasmonic biosensor with gold and titanium dioxide immobilized on photonic crystal fiber for blood composition detection, IEEE Sens. J. **22**, 9 (2022).

[6] J. B. Pendry, D. Schurig D, and R. Smith, Controlling electromagnetic fields, Science **312**, 5784 (2006).

[7] N. F. Yu and F. Capasso, Flat optics with designer metasurfaces, Nat. Mater. **13**, 2 (2014).

[8] G. Minatti, F. Caminita, M. Casaletti, and S. Maci, Spiral leaky-wave antennas based on modulated surface impedance, IEEE Trans. Antennas Propag. **59**, 12 (2011).

[9] K. Achouri, M. A. Salem, and C. Caloz, General metasurface synthesis based on susceptibility tensors, IEEE Trans. Antennas Propag. **63**, 7 (2015).

[10] P. Cheben, R. Halir, J. H. Schmid, H. A. Atwater, and D. R. Smith, Subwavelength integrated photonics, Nature **560,** 7720 (2018).

[11] T. J. Cui, M. Q. Qi, X. Wan, J. Zhao, and Q. Cheng, Coding metamaterials, digital metamaterials and programmable metamaterials, Light: Sci. Appl. **3,** 10 (2014).

[12] J. B. Pendry, L. Martin-Moreno, and F. J. Garcia-Vidal, Mimicking surface plasmons with structured surfaces, Science **305,** 847 (2004).

[13] X. Shen, T. J. Cui, D. Martin-Cano, and F. J. Garcia-Vidal, Conformal surface plasmons propagating on ultrathin and flexible films, Proc. Nat. Acad. Sci. U. S. A. **110,** 40 (2013).

[14] P. H. He, H. C. Zhang, W. X. Tang, Z. X. Wang, R. T. Yan, and T. J. Cui, A multi-layer spoof surface plasmon polariton waveguide with corrugated ground, IEEE Access **5,** 25306 (2017).

[15] A. Kianinejad, Z. N. Chen, C. Qiu, Full modeling, and loss reduction, and mutual coupling control of spoof surface plasmon-based meander slow wave transmission lines, IEEE Trans. Microwave Theory Tech. **66,** 3764 (2018).

[16] H. C. Zhang, P. H. He, W. X. Tang, Y. Luo, and T. J. Cui, Planar spoof SPP transmission lines, IEEE Microwave Mag. **20,** 73 (2019).

[17] H. C. Zhang, P. H. He, X. Gao, J. Lu, T. J. Cui, and Y. Luo, Loss analysis of plasmonic metasurfaces using field-network-joint method, IEEE Trans. Antennas Propag. **67,** 5 (2019).

[18] P. H. He, H. C. Zhang, X. Gao, L. Y. Niu, W. X. Tang, J. Lu, L. P. Zhang, and T. J. Cui, A novel spoof surface plasmon polariton structure to reach ultra-strong field confinements, Opto-Electron. Adv. **2,** 190001 (2019).

[19] P. H. He, D. Y. Yao, H. C. Zhang, J. P. Wang, D. Bao, and T. J. Cui, Ultra-compact on-chip spoof surface plasmon polariton transmission lines with enhanced field confinements, J. Phys.: Photonics **4,** 4 (2022).

[20] H. C. Zhang, S. Liu, X. Shen, L. H. Chen, L. Li, and T. J. Cui, Broadband amplification of spoof surface plasmon polaritons at microwave frequencies, Laser Photonics Rev. **9,** 83 (2015).

[21] P. H. He, L. Y. Niu, Y. Fan, H. C. Zhang, P. L. Zhang, D. Y. Yao, W. X. Tang, and T. J. Cui, Active odd-mode-metachannel for single-conductor systems, Opto-Electron. Adv. **5,** 8 (2022).

[22] H. C. Zhang, Y. Fan, J. Guo, X. Fu, and T. J. Cui, Second-harmonic generation of spoof surface plasmon polaritons using nonlinear plasmonic metamaterials, ACS Photonics **3,** 1 (2015).

[23] L. Y. Niu, P. H. He, Y. Fan, P. L. Zhang, H. C. Zhang, and T. J. Cui, Gain-associated nonlinear phenomenon in single-conductor odd-mode plasmonic metamaterials, Laser Photonics Rev. **16,** 6 (2022).

[24] D. F. Guan, P. You, Q. Zhang, K. Xiao, and S. W. Yong, Hybrid spoof surface plasmon polariton and substrate integrated waveguide transmission line and its application in filter, IEEE Trans. Microwave Theory Tech. **65,** 4925 (2017).

[25] H. C. Zhang, P. H. He, X. Gao, W. X. Tang, and T. J. Cui, Pass-band reconfigurable spoof surface plasmon polaritons, J. Phys.: Condens. Matter **30,** 134004 (2018).

[26] D. F. Guan, P. You, Q. Zhang, Z. B. Yang, H. Liu, and S. W. Yong, Slow-wave half-mode substrate integrated waveguide using spoof surface plasmon polariton structure, IEEE Trans. Microwave Theory Tech. **66,** 2946 (2018).

[27] A. Aziz, Y. Fan, P. H. He, H. C. Zhang, Irshad Ali, W. X. Tang, and T. J. Cui, Spoof surface plasmon polariton beam splitters integrated with broadband rejection filtering function, J. Phys. D: Appl. Phys. **54,** 335105 (2021).

[28] Y. J. Han, Y. F. Li, H. Ma, J. F. Wang, D. Y. Feng, S. B. Qu, and J. Q. Zhang, Multibeam antennas based on spoof surface plasmon polaritons mode coupling, IEEE Trans. Antennas Propag. **65,** 1187 (2017).

[29] A. Kianinejad, Z. N. Chen, and C. W. Qiu, A single-layered spoof-plasmon-mode leaky wave antenna with consistent gain, IEEE Trans. Antennas Propag. **65,** 681 (2017).

[30] Y. J. Lu, H. C. Zhang, P. H. He, L. P. Zhang, and T. J. Cui, Design of miniaturized antenna using corrugated microstrip, IEEE Trans. Antennas Propag. **68,** 1918 (2020).

[31] Z. W. Cheng, H. F. Ma, M. Wang, and T. J. Cui, Dual-beam leaky-wave radiations with independent controls of amplitude, angle, and polarization based on SSPP waveguide, Adv. Photonics Res. **3,** 2100313 (2022).

[32] P. H. He, Y. Ren, C. Shao, H. C. Zhang, L. P. Zhang, and T. J. Cu, Suppressing high-power microwave pulses using spoof surface plasmon polariton mono-pulse antenna, IEEE Trans. Antennas Propag. **69,** 8069 (2020).

[33] G. S. Kong, H. F. Ma, B. G. Cai, and T. J. Cui, Continuous leaky-wave scanning using periodically modulated spoof plasmonic waveguide, Sci. Rep. **6,** 29600 (2016).

[34] J. Y. Han, J. Wang, S. Gong, Y. Li, Y. Zhang, and J. Zhang, Low RCS antennas based on dispersion engineering of spoof surface plasmon polaritons, IEEE Trans. Antennas Propag. **66,** 2094 (2018).

[35] P. H. He, Y. Fan, L. Y. Niu, H. C. Zhang, C. Y. Wei, J. Zhang, H. Gao, Y. Huang, J. Xu, W. Tang, and T. J. Cui, Analysis, reduction, and utilization of loss in reconfigurable spoof surface plasmon polaritons, IEEE Trans. Microwave Theory Tech. **71,** 945 (2023).

[36] H. C. Zhang, T. J. Cui, Y. Luo, J. Zhang, J. Xu, P. H. He, and L. P. Zhang, Active digital spoof plasmonics, Natl. Sci. Rev. **7,** 261 (2020).

[37] L. P. Zhang, C. H. Zhang, M. Tang, H. P. He, Y. L. Niu, L. Liu, Y. J. Lu, X. W. Tang, F. J. Mao, and J. T. Cui, Integrated multi-scheme digital modulations of spoof surface plasmon polaritons, Sci. China Inf. Sci. **63,** 202302 (2020).

[38] W. Y. Cui, J. Zhang, X. Gao, and T. J. Cui, Reconfigurable Mach-Zehnder interferometer for dynamic modulations of spoof surface plasmon polaritons, Nanophotonics **11,** 1913 (2021).

[39] X. Tian, P. M. Lee, Y. J. Tan, Tina L. Y. Wu, H. C. Yao, M. Y. Zhang, Z. P. Li, Kian Ann Ng, Benjamin C. K. Tee, and John S. Ho, Wireless body sensor networks based on metamaterial textiles, Nat. Electron. **2,** 6 (2019).

[40] H. C. Zhang, P. L. Zhang, P. H. He, J. Xu, C. Qian, F. J. Garcia-Vidal, and T. J. Cui, A plasmonic route for the integrated wireless communication of subdiffraction-limited signals, Light: Sci. Appl. **9,** 1 (2020).

[41] P. H. He, Y. Fan, H. C. Zhang, L. P. Zhang, M. Tang, M. N. Wang, L. Y. Niu, W. X. Tang, and T. J. Cui, Characteristic impedance extraction of spoof surface plasmon polariton waveguides, J. Phys. D: Appl. Phys. **54**, 385102 (2021).

[42] Louis E Frenzel, *Principles of electronic communication systems* (McGraw-Hill, Boston, USA, 2007).

[43] Xin Hu, Qiaoli Zhang, and Sailing He, Dual-band-rejection filter based on split ring resonator (SRR) and complimentary SRR, Microwave Opt. Technol. Lett. **51**, 2519 (2009).

[44] S. Zhao, H. C. Zhang, J. Zhao, and W. X. Zhao, An ultra-compact rejection filter based on spoof surface plasmon polaritons, Sci. Rep. **7**, 1 (2017).